Edinburgh Research Explorer

Fuel Cell Modeling and Optimization

Chapter 3

Fuel cell modeling and optimization

Lei Xing[1,*], Xueguan Song[2] and Prodip K. Das[3]

[1]*School of Chemistry and Chemical Engineering, University of Surrey, Guildford, United Kingdom, *[2]*State Key Laboratory of High-Performance Precision Manufacturing, School of Mechanical Engineering, Dalian University of Technology, Dalian, P.R. China,* [3]*School of Engineering, The University of Edinburgh, Edinburgh, United Kingdom*

Abstract:

As a highly efficient and cost-saving approach, modeling is significantly important in the development of proton exchange membrane fuel cells (PEMFCs). With the rapid development of computer technologies in the past three decades, PEMFC models have been upgraded from simple one-dimension (1D) single-cell models to sophisticated three-dimension (3D) multi-physics and multi-phase fuel-cell stack models, leading to the wider application of modeling in the diagnosis, design, optimization, and development of novel PEMFCs. This chapter provides the chronological development of PEMFC modeling approaches with a focus on those in modeling the catalyst layer and water formation and transport inside the PEMFCs. Numerical optimizations of PEMFCs with respect to electrodes, flow fields, fuel cell stacks, and operating conditions are summarised. The multi-variable optimization and data-driven modeling are also introduced in this chapter.

Key Words: Modeling, Optimization, Graded design, Flow field design, Surrogate model

---

* Corresponding author: L.Xing@surrey.ac.uk

1. Introduction

Modeling plays a significant role in the process of proton-exchange-membrane and related fuel cell design and development [1]. Normally, fuel cell design and development processes begin with a set of requirements, including power output, operating conditions, size limitations, safety specifications, and others. Based on the knowledge of materials and processes involved in the fuel cells, modeling is performed to predict the fuel cell performance. Modeling helps the designers and developers to determine the best candidate designs or improve the existing designs that satisfy the requirement. Modeling provides a better understanding of the electrochemical reactions and mass transport that occurred within the fuel cells, for example, the reactants profiles, temperature distribution, and polarisation curves [2-5]. It can give a quick prediction of the fuel cell performance under various given operating conditions, material properties, and fuel cell geometries. Modeling reduces the time, effort, and cost associated with the experimental studies, and provides theoretical guidance on the development and optimization of the fuel cells.

The processes that occurred inside the porous electrode of proton exchange membrane fuel cells (PEMFCs) constitute a fully coupled reaction-diffusion process. Due to the competitive relationship between the electrochemical reaction and species transport [6], optimal cell performance requires graded distributions of the functional compositions inside the electrodes and novel flow fields, where the optimal parameters for maximized cell performance, e.g., platinum (Pt) loading, ionomer loading, porosity and hydrophobicity of the electrodes, vary according to the different operational requirement of PEMFCs. The optimal distributions of different functional components and novel flow field design could be achieved through multi-variable optimization approaches. Thus, modeling and optimization could accelerate the commercialization and industrialization of PEMFC technology.

2. Fuel cell modeling approach and key physicochemical and operating parameters

A complete PEMFC model includes several sub-models, including gas flow, mass and heat transport, mechanical properties of the electrodes, water transport through the membrane, gas-liquid two-phase flow, proton, and electron transport, reaction kinetics and current distributions, as shown in Figure 3.1. The interaction of different sub-models describes the computational process in solving a completed PEMFC model. To reduce the complexity of the model, several sub-models are typically excluded. For example, when heat transfer is omitted, a PEMFC model becomes an isothermal model. When the generation and transport of liquid water are neglected, the PEMFC model can be simplified to a single-phase flow model. In most PEMFC models, the gas flow, mass transport, and current distribution are essential. Key operating

parameters include inlet gas velocity, relative humidity, operating pressure, temperature and cell voltage. To reflect the catalytic activity and mass and ion transport resistance of the porous electrode, Pt-loading, platinum and carbon mass ratio, ionomer volume fraction, conductivity, porosity, and electrode thickness are also important. The governing equations describing fluid momentum, diffusive and convective mass transport, electrochemical reaction kinetics, and heat transport could be found in Chapter 2. Different from other high-temperature fuel cells, water management is critical in low-temperature fuel cells, which are typically operated below 100°C. The following sections focus on the modeling of water formation and transport of PEMFCs.
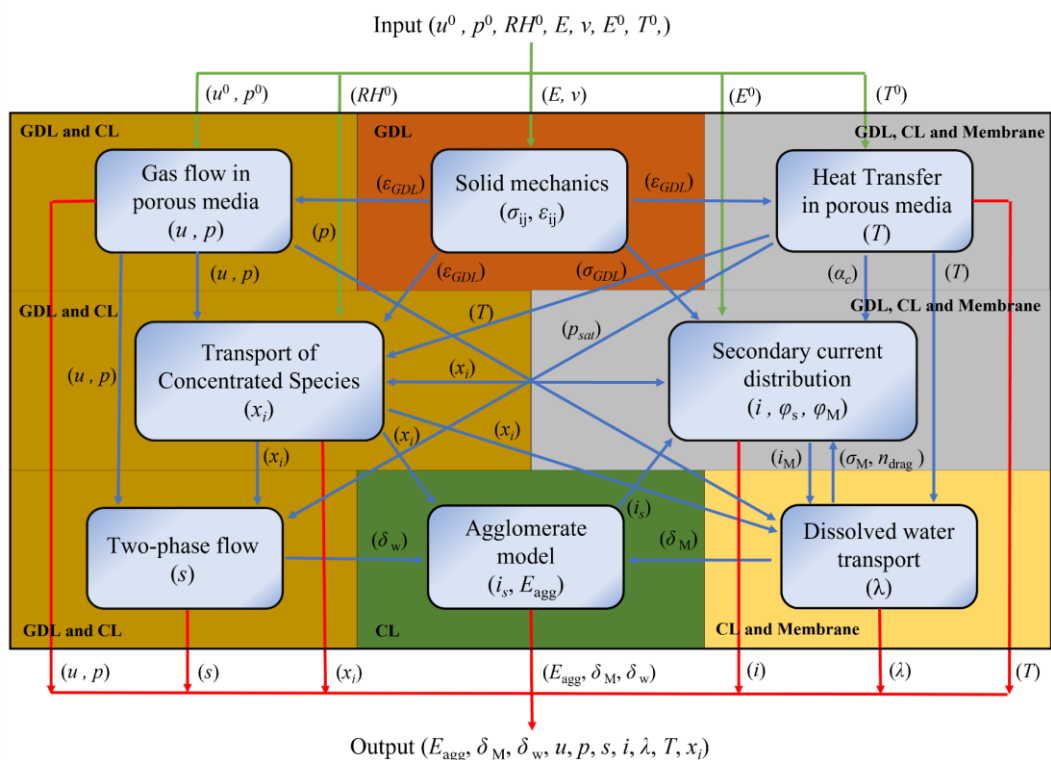
FIGURE 3.1 Schematic computational process in solving a multi-physics, non-isothermal, multi-phase flow model of a PEMFC. Symbols have their usual meanings and are described in Chapter 2.

2.1 Water formation and transport in fuel cells

Perfluorinated membranes, such as Nafion®, are typically used as the electrolyte in PEMFCs. Nafion® ionomer is required in the catalyst layers (CLs) to facilitate proton transport from the anode CL, through the membrane, to the cathode CL. On the membrane-CL boundary, the membrane is closely connected with the ionomer in the CLs, at both the anode and cathode. Water in PEMFCs acts as the lubricant which makes the fuel cell system run smoothly at a relatively low ionic resistance. Water can be fed into the PEMFC system through the gas inlet or/and generated by the oxygen reduction reaction (ORR) at the cathode. Water exists as water

vapor in the gas mixture, which is absorbed by the Nafion® membrane/ionomer as the dissolved water. During fuel cell operation, protons migrate through the membrane and are associated with a drag of water molecules from the anode to the cathode, which is the electro-osmotic drag (EOD). Together with the electrochemical water production, the water content of the membrane/ionomer becomes saturated, which then leads to liquid water formation through membrane/ionomer desorption when the water content exceeds the equilibrium value. The other reason for water formation is attributed to vapor condensation when the partial pressure of vapor exceeds the equilibrium vapor pressure at a given temperature. Due to the generated gradient of water concentration between the anode and cathode, a certain amount of water could diffuse back from the cathode to the anode, which is in the opposite direction against the EOD. In addition, the pressure difference between the anode and cathode could drive water transport through the membrane, which is called hydraulic permeation. The water transport that occurred in a PEMFC is schematically shown in Figure 3.2.
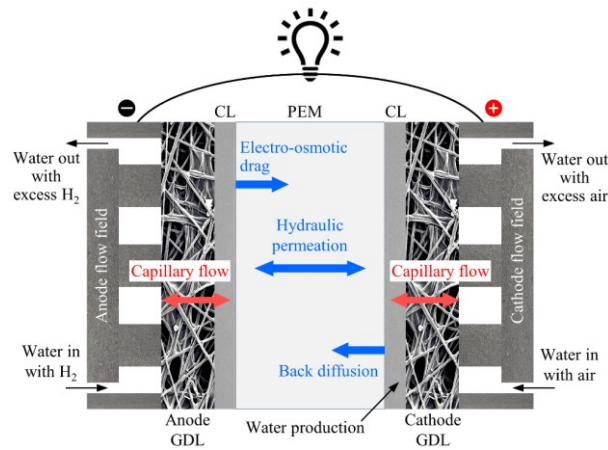

FIGURE 3.2 Water transport mechanism inside a proton-exchange-membrane fuel cell.

Maintaining a subtle equilibrium between membrane dehydration and liquid water flooding is the key issue to achieving maximum performance and durability for PEMFCs [7]. On one hand, water is required to guarantee the good proton conductivity of the proton exchange membrane and ionomer of CLs [8]. Dehydrated membrane/ionomer hinders the access of protons to the active sites within the CL, resulting in an increase in activation polarisation [9]. On the other hand, excess water blocks the flow channel and the void space within the porous electrodes and then increases the mass transport resistance, leading to a 'flooding' problem. The thickness of the membrane, the water content of the membrane, the humidity of the reactant gases, and the reaction rate in CL determine the concentration gradient of water between the anode and cathode. Furthermore, membrane water content and reactant gas humidity are dependent on the gas inlet humidification and the temperature and pressure in the gas channels [10]. Besides, back diffusion prevails over electro-osmotic drag at lower current density; and electro-osmotic

drag prevails over back diffusion while higher current density is achieved, thus the anode (including the membrane) tends to dry out, even the cathode is well hydrated at high current density [11].

2.2 PEMFC modeling approaches

Numerical modeling of PEMFCs is important for a better understanding of the transport processes owing to the experimental drawbacks, such as the difficulty of performing the different experimental measurements simultaneously, unrealistic operating conditions, and the high cost of materials and testing instruments. Over the last decades, numerous models and studies have been conducted to describe water management and investigate liquid water transport in PEMFCs [12-18]. Depending on different descriptions of water formation and transport, the models can be mainly categorized into four groups: dynamic models, lumped models, flooding models, and models associated with the effect of geometrical configuration.

In the early 1990s, some simple models have been developed. These models were all simplified models which all applied the assumption that the reactant and charge only transport along one direction. The numerical models developed by Springer et al. [19, 20] and Bernardi and Verbrugge [21, 22] are usually considered pioneering modeling works for PEMFCs. These models are essentially one-dimensional (1D) models considering the membrane, CL, and gas diffusion layer (GDL) based on solving the conservation equations by assuming homogeneous materials and using effective transport properties. After that, Nguyen and White [23] and Fuller and Newman [24] developed pseudo-two-dimensional (2D) models by further considering the flow channels, which considered the effect of water humidity inlet and temperature distributions, providing more detailed water and thermal management capability. However, the models developed in that period were too simple to simulate the very complex PEMFC systems although they laid the foundation for fuel cell modeling.

More numerical models were developed in the late 1990s. For instance, Yi and Nguyen [25, 26] and Gurau et al. [2] developed 2D models to explore more detailed transport phenomena in PEMFCs. These models illustrated the utility of multi-dimensional models in the understanding of the internal conditions of fuel cells, such as the reactant and water distribution. Gloaguen and Durand [27], Bultel et al. [28-30], and Marr and Li [31] developed the agglomerate models. These models applied simplified CL structures by assuming that the large agglomerates were formed by ionomer and platinum/carbon particles on the level of a micrometer. Compared to the models developed earlier, more detailed mass and charge transport phenomena were analyzed more accurately because these models extended the 1D or pseudo-2D to the detailed 2D models. It is important to note that all the models developed were based on the single-phase assumption, which treated the water as vapor, including the water formed in the cathode CL,

and supplied it along with the humidified gas inlet. The water condensation within the porous electrodes and the flow channels was not considered. Although there was not sufficient evidence to confirm that water could be condensed in CLs and GDLs while the PEMFC system operated in normal conditions, however, condensed water in the flow channels has been observed by some instruments such as high-resolution cameras [32, 33]. Generally, an ideal single-phase assumption is applied when reactant gases are oxidised or reduced at the surface of a solid catalyst (Pt-Ru and other binary or ternary alloy). In reality, the condensed water could change the single-phase flow problem to a two-phase flow problem.

In the 2000s, multi-dimensional models have been developed by many researchers to solve a complete set of conservation equations (such as continuity and Navier-Stokes) coupled with electrochemical reactions (for example the ORR kinetics at the cathode). Computational fluid dynamics (CFD) code and commercial software (such as ANSYS Fluent, and COMSOL Multiphysics) based on finite volume methods (FEM) were adopted to develop the fuel cell models, and more complicated geometry and transport phenomena were investigated [34-44]. In the area of three-dimensional (3D) geometry, the models developed by Dutta et al. [34, 35], Zhou and Liu [36], Berning et al. [37], Mazumder and Cole [38], Lee et al.[40], Um and Wang [41], and Wang and Wang [42] were mainly considered a single flow channel with the major components of reactant gases. Large-scale simulations considering multi-channel or small stacks give a more accurate and more specific analysis of the distribution of reactant gases (H_2 and O_2), water vapor, and pressures. [45-48]. The main impediment to the widespread use of these multi-dimensional models is the requirement for computer hardware.

A reasonable simplification of the complex multi-dimensional models is considered the practical way of modeling the complicated transportation and reaction inside of the PEMFCs with the relatively low computational requirement. To simplify models and reduce computation time for conservation equations, liquid water formation can be neglected by assuming liquid water as supersaturated water vapor [23-25]. The real two-phase flow models, which give more accurate predictions than the single-phase assumptions, have also been developed [39, 49-55]. These two-phase flow models solved the mass, momentum, and species transport conservation equations for the gas mixture, with an extra conservation equation for liquid water transport. However, the accurate and detailed water transport behavior cannot be studied in these models because the interface tracking between liquid water and gas is not permitted. As a result, the volume of fluid (VOF) model, based on liquid water dynamics to investigate water flow in a single serpentine flow channel, was developed [56]. The real 3D model is difficult to simulate a single cell with a large size due to the expensive computations. Therefore, many researchers simplified the sub-models of CLs and developed a "3D+1D" model to improve the computational efficiency by approximately one order of magnitude. This model can be

employed to help develop the large-size flow fields of PEMFCs. For example, Xie et al. [57] developed a "3D+1D" PEMFC model to implement large-scale simulation with enhanced calculation efficiency, in which bipolar plates, gas channels, and gas diffusion layers were treated as 3D computational domain and micro-porous layers, CLs, and membrane are treated as 1D domain. The computation time was reduced by 20 folds for large-scale PEMFCs with 345 cm^2 active area. In their later work [58], the accuracy of the developed "3D+1D" PEMFC model was comprehensively validated in terms of overall cell performance and local distributions of current density and temperature under different operating conditions. This approach provided some guidance for researchers and engineers in the field of PEMFC design by facilitating the application of 3D modeling and simulation to large-scale PEMFCs.

In short, a large number of numerical models were developed around the world and the models were chronologically developed from simple to complex, from general to specific. Despite the great changes in the equation forms in the models, all the processes are described based on some basic laws, e.g., the laws of conservation of energy and momentum. Developing a comprehensive and comparatively simple model for the PEMFCs under practical load conditions by reasonably simplifying the complex multi-dimensional models is the priority of most modeling work. The main difference between the models developed in different periods is presented in Table 3.1.

Table 3.1 Chronological development of PEMFC modeling work.

Models	Period of development	Dimensions of reactant, products and charge transportation	Accuracy of modeling process compared to practical fuel cell	Complexity of the models and computer hardware requirement
1D and pseudo 2D	Early 1990s	One dimensional	Crude	Simple and low
2D	Later 1990s	Two dimensional	Medium	Medium
3D and multi-dimensional	After 2000s	Three dimensional	Precise	Complex and high

2.3 Modeling of water transport through the membrane

The modeling of water transport in the membrane can be classified into three types: diffusive, chemical potential, and hydraulic models. The diffusive model can be explained with dilute solution theory by considering the membrane as a solvent, while water and proton as solutes.

This theory assumes that the interaction between different solute species can be neglected, and only the interaction between solute (water and proton) and solvent (membrane) is considered. Then the flux of solute species in the solvent can be described by using the Nernst-Planck equation. The Nernst-Planck equation is a conservation of mass describing the flux of ions under the influence of both an ionic concentration gradient and an electric field. The general form of the Nernst-Planck equation is:

$$\frac{dc_i}{dt} = \nabla \left(D_i \nabla c_i - \mathbf{u} c_i + \frac{D_i z_i e}{k_B} c_i \nabla \varphi \right) \tag{3-1}$$

where t (s) is time, D_i (m^2 s^{-1}) is the diffusivity of the solute species i, c_i (mol m^{-3}) is the concentration of the solute species i, $\mathbf{u}$ (m s^{-1}) is the velocity of the fluid, z_i (C) is the valence of ionic specie, k_B (J K^{-1}) is the Boltzmann constant, and φ (V) is potential.

For water transport, $D_i z_i e c_i \nabla \varphi / k_B$ becomes zero because water is in zero valence. For proton transport, $D_i \nabla c_i$ becomes zero by assuming a constant concentration of proton through the membrane. Furthermore, $\mathbf{u} c_i$ becomes zero for both the water and proton transport because the membrane does not move. Therefore, the Nernst-Planck equation for proton transport is simplified to Ohm's law. By further considering the effect of electro-osmotic drag, the water transport is simplified to [59]:

$$J_w = D_M \nabla c_w + n_{drag} \frac{i}{F} \tag{3-2}$$

where D_M (m^2 s^{-1}) is the diffusivity of water through the membrane, c_w (mol m^{-3}) is water concentration, n_{drag} is electro-osmotic drag coefficient through the membrane, F (C mol^{-1}) is Faraday's constant, and i (A m^{-2}) is the current density.

The diffusive model is the most successful model for water transport through membrane since its initial application [19, 20]. By further considering the interaction between different solute species, the chemical potential model is developed. The proton and water transport through the membrane, therefore, can be explained by concentrated solution theory as [60, 61]:

$$i = -\sigma_M \nabla \phi - \frac{n_{drag} \sigma_M}{F} \nabla \prod_H \tag{3-3}$$

$$J_w = -\alpha_w \nabla \prod_w + n_{drag} \frac{i}{F} \tag{3-4}$$

where σ_M (Ω^{-1}) is the membrane conductivity, $\prod_H$ (J mol^{-1}) and $\prod_w$ (J mol^{-1}) are the chemical potential of proton and water, respectively, and α_w is the water transport coefficient through the membrane.

Comparison of Eq. (3-2) and Eq. (3-4) shows that the concentration (c) is replaced by chemical potential ($\prod$), the diffusion coefficient (D) is replaced by transport coefficient (α), and one more term is added in Eq. (3-3) to account for the multi-component interaction. The biggest obstacle to the widespread use of the chemical potential model is the difficulty in obtaining the transport parameters. As a result, the chemical potential model is rarely used in comparison with the diffusive model.

In the diffusive and chemical potential models, the convective transport caused by the pressure gradient across the membrane is not considered. However, convective transport could happen when water enlarges the pores of the membrane. To fill the gap, the hydraulic model is developed [21, 22]. Consequently, water flux due to pressure gradient and EDO can be calculated by the Nernst-Planck equation. Generally, the hydraulic model neglects the diffusive transport, and the water flux can be represented by the following equation:

$$J_w = -c_w \frac{k_p}{\mu_w} \nabla p_w + n_{drag} \frac{i}{F} \tag{3-5}$$

where k_p (m^2) and μ_w (Pa s) are the permeability and dynamic viscosity of water in the membrane. Due to the effect of EDO, the anode side of the membrane is often prone to dry out. Therefore, the fully hydrated membrane assumption remains questionable. In fact, water convective transport is only considerable while the pressure gradient exists between the anode and cathode. If the inlet gas pressure of the anode is as same as that of the cathode, the water convective transport could be neglected because diffusive transport and EDO have a more significant influence on the water transport.

2.4 Modeling of water transport through porous electrodes

Depending on the assumption of the morphology of the porous electrodes, models of the water transport through the porous electrodes can be categorized into 'homogenous' and 'non-homogenous' models. In the homogenous model, the porous electrodes are assumed to be constructed by homogeneous materials, while the non-homogenous model applies the real or simplified microstructure of the porous electrodes. When the porous electrodes are assumed as homogeneous, the entire computational domain shares the same properties, such as conductivity, permeability, and porosity. The overall effect of the micro-structure is usually reflected by the effective coefficient. Thus, the geometry generation and the model solving

process are greatly simplified and result in easier model development and lower requirement of the computer hardware. The disadvantage of this assumption is the lack of precision about the detailed process within the porous electrodes, such as nucleation water. The modeling works before the 2000s usually adopt the homogeneous assumption [2, 15, 16, 19-30]. The GDL is typically made up of three-dimensional random carbon fiber and its real structure is highly anomalous [62-64]. To accurately simulate the electrochemical reactions and transport processes that occurred in a real or simplified GDL, e.g. liquid water formation and transport, numerous models have been developed, including the volume of fluid (VOF) model [10, 41, 42, 55, 65-67] and Lattice Boltzmann (LB) model [68-71]. The details of the VOF approach could be found in Chapters 2 and 13.

2.5 Catalyst layer modeling

The CLs are the core of a PEMFC, in which electrochemical reactions occurred. The CLs are prepared by spraying the catalyst particle (such as Pt-Ru alloy) contained ink onto the carbon paper. The difference between the CL and other layers is that the catalyst particle is surrounded by the carbon fiber in the catalyst layers and results in much smaller pores than that of the GDLs. Therefore, the VOF model is hard to be applied to the microstructure of the CLs [62]. The general process of the electrochemical reaction includes two steps, diffusion, and reaction. First of all, the reactants must transport through the porous media and ionomer films and reach the surface of the catalyst particles. Then the reactants are absorbed on the surface of the catalyst particle where products are generated via chemical reactions. Finally, the products generated on the surface of the catalyst particle must move away. The modeling approaches applied on the catalyst layer, depending on the degree of complexity, can be categorized into three groups. In the simplest approach, the CLs are treated as reactive boundaries between the GDL and membrane [37, 72]. For example, Jeng et al. [72] developed a simple 2D across-the-channel model to study the mass transport of the reactant gases through the GDLs. The effectiveness of the GDLs was evaluated under different current densities and an optimal thickness of the cathode GDL was suggested. Berning et al. [37] developed a 3D, non-isothermal model to investigate the temperature distribution in the MEA. However, the catalyst layers were treated as 1D boundaries in this model. It is important to notice that this kind of approach often overestimates the current density due to the ignorance of the mass transport resistance in the catalyst layer. The second approach assumes the CL as a thin film fully flooded with liquid water [31] or the existence of a flooded interface between the GDL and CL [73]. The 'thin-film-fully-flooded' approach is adopted in the model developed by Marr and Li [31], in which the void space within the cathode CL was fully occupied by liquid water. The 'flooded-interface' approach is adopted in the analytical model developed by Das et al. [73]. These approaches led to reasonable simulation results of the cell at higher current densities. However, it

underestimates the cell performance at lower current densities due to an increase in mass transport resistance within the CL. The most accurate approach to CL modeling is the agglomerate model, in which the CL is assumed as a porous 2D or 3D domain filled with Pt/C catalyst particles agglomerate surrounded by thin ionomer films [74-78]. The void spaces within the agglomerates (intra-agglomerate space) and between the agglomerates (inter-agglomerate space) are defined as the primary and secondary pores, respectively. Both the primary and secondary pores can be filled with ionomer, liquid water, and reactants. The agglomerate models can be further subcategorized into three sub-groups namely slab, cylindrical, and spherical agglomerate models [63].

To give a more accurate simulation of the diffusion-reaction process that occurred in the catalyst layer, agglomerate models are usually preferred. In the agglomerate models, the catalyst particles, ionomer, and void space are assumed to be homogeneously mixed to form the micrometer agglomerates. In the spherical agglomerate model, the diameter of the agglomerate can be less than 10 μm [64]. The agglomerate models are usually adopted to describe the relatively sluggish ORR of the cathode CL of PEMFCs.

3. Numerical optimization of PEMFCs

Numerical optimization has been an active research area since the 1960s. It has been used in many applications. The common principle of numerical optimization is to efficiently search for an optimal design in a coupled mathematical algorithm with the aid of a computational analysis tool. Only a few designs need to be evaluated using the optimization algorithm, the computational time is therefore reduced. Optimal design helps researchers to create a new design or improve an existing one. To account for the inter-relationship between various parameters and optimize several objectives simultaneously in a fuel cell design, multi-objective optimization is always used. A mathematical formulation of such a problem is given by:

Maximize or minimize $\quad\quad \mathbf{J(x)} = [J_1, J_2, J_3, ..., J_n]^T$

W.R.T $\quad\quad\quad\quad\quad\quad x_k \quad$ for $k = 1, 2, 3, ..., n$

Subject to: $\quad\quad\quad\quad\quad h_i(\mathbf{x}) = 0 \quad$ for $\quad i = 1, 2, 3, ..., p \quad\quad\quad\quad\quad$ (3-6)

$\quad\quad\quad\quad\quad\quad\quad\quad\quad g_i(\mathbf{x}) \leq 0 \quad$ for $\quad i = 1, 2, 3, ..., q$

$\quad\quad\quad\quad\quad\quad\quad\quad\quad \mathbf{x}_L \leq \mathbf{x} \leq \mathbf{x}_U$

where $\mathbf{J(x)}$ is the vector of objectives. In fuel cell design, the objective can be cost, performance, durability and others, which is represented by J_i individually. x_k is known as the design variables, which are related to the objective vector, $\mathbf{J(x)}$. $\mathbf{x}_L$ and $\mathbf{x}_U$ are the lower and upper bounds of the design variable x_k. $h_i(\mathbf{x})$ and $g_i(\mathbf{x})$ are the design constraints.

The design of fuel cells is a challenging endeavor because the multitude of physical and chemical phenomena need to be optimized simultaneously to achieve the best performance. Normally, it requires the evaluation of a set of possible designs. Due to the fact that the number of possible designs increases sharply as the number of design variables increases. For example, the number of possibilities is 10^5 for a design with ten variables and five possibilities per variable. It is impossible to evaluate all possible designs. As a result, some design variables have to be constrained as constants to reduce the number of possible designs. This is the so-called sub-optimal design. The sub-optimal designs in fuel cell optimization mainly focus on the following aspects: electrode design, flow field design, fuel cell stack, and operating condition optimization. Similarly, the optimization has to mainly concentrate on limited important objectives, while ignoring other design objectives.

Numerical optimization could provide insight into fuel cell design including cost reduction, performance improvement, and efficiency increment. As a relatively new research area, numerical optimization of needed fuel cells has attracted growing interest.

3.1 Elecrode optimization

During PEMFC's operation, the electrochemical reaction and reactant mass transport are fully coupled and the overall rate is determined by the slowest process. The detailed mass transfer in porous electrodes is discussed in Chapter 13. While higher catalyst loading increases reaction activity and reduces activation overpotentials [79], it also reduces reactant transport and liquid-water capacity inside the catalyst layer. It was shown in Ref. [79] that the catalyst loading of 0.3 mg cm^{-2} or higher has limited or no change in activation overpotential. Thus, the functional components of the porous electrode must be optimized to achieve maximum cell performance. Holdcroft's group is considered the pioneer in the optimization of the fuel cell electrode using a numerical optimization approach [80, 81]. The CL composition was optimized to achieve the maximum current density at the cell voltage of 0.6 V. The design variables were ionomer volume fraction, Pt-loading, and CL thickness. The optimal distributions of Nafion® ionomer and platinum were obtained. The optimization results indicated that the optimal ionomer loading was around 30 wt.% [80], and the electrode performance was improved by placing more ionomer and platinum near the membrane [81]. Das et al. [73] developed a single-objective analytical approach using the exact solution of activation overpotential for cathode CL's optimization. The CL composition (ionomer and platinum loadings) and thickness were optimized to achieve maximum power density at a given cell voltage for both air and oxygen.

It was found that Pt-loading of about 0.2 mg cm^{-2} can provide optimum performance at 0.8 V, which is in line with the conclusion of Song et al. [80] at 0.6 V. The optimum CL thickness with a Pt-loading of 0.2 mg cm^{-2} was found to be between 9 and 11 microns at the cell voltage of 0.8 V. However, the optimum CL thicknesses vary between 9 and 16 microns depending upon Pt-loadings.

Conversely, Secanell et al. optimized both Pt-loading and the performance of a complete MEA [82] based on the previously developed optimization framework [83]. The design variables included Pt-loading, ionomer loading, GDL porosity, and platinum mass ratio. Figure 3.3 shows the optimization of Pt-loading and CL thickness (for various Pt-loadings) at the cell voltage of 0.8 V of Ref. [73] and the polarisation curves of the base-case design and optimal design at the cell voltage of 0.676 V and 0.476 V of Ref. [83]. Figure 3.3 shows that the cell performance was improved using the parameters obtained from the optimal design. The optimization results showed that Pt-loading had to be controlled within the range of 0.1 to 0.5 mg cm^{-2}, as higher loading resulted in a waste of platinum rather than an increase in current density.
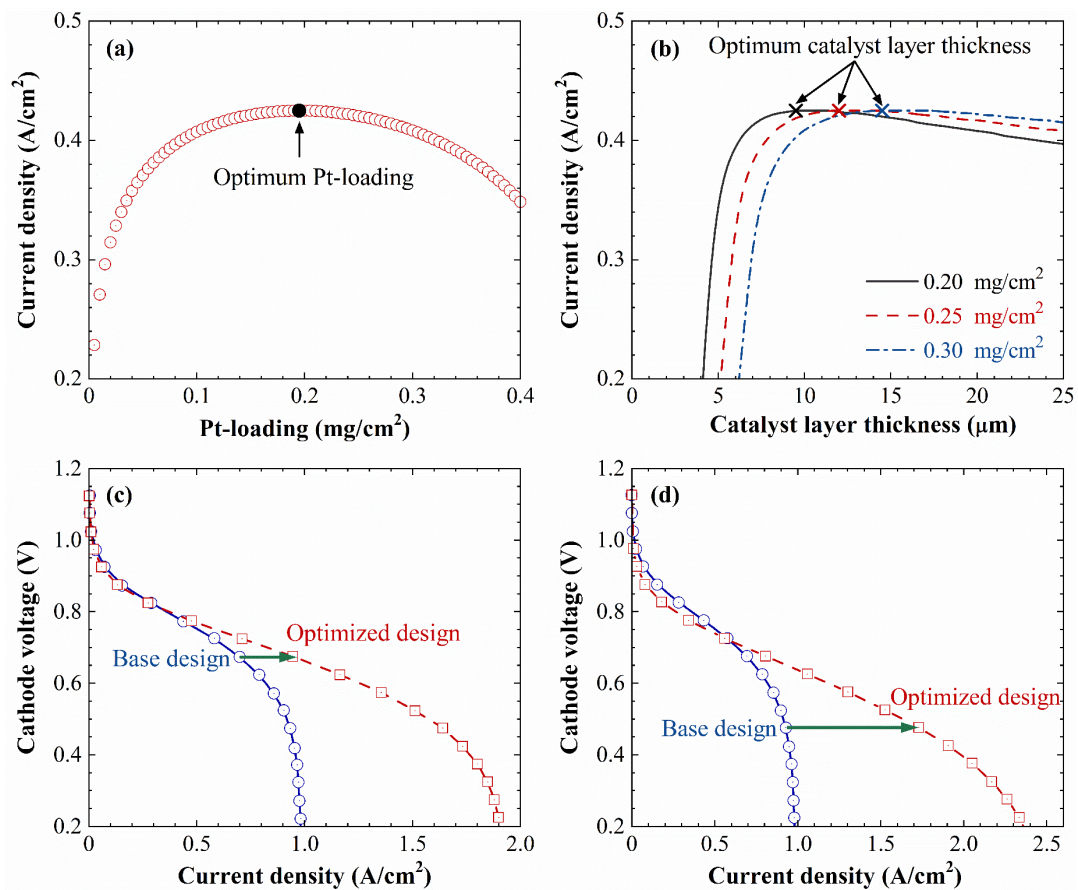

FIGURE 3.3 Optimization of Pt-loading and catalyst layer thickness at the cell voltage of 0.8 V (parts (a) and (b)) and polarisation curves of the base-case design and optimal design at the cell voltage of 0.676 V and 0.476 V (parts (c) and (d)). *Data for parts (a) and (b) are taken from Ref. [73] and parts (c) and (d) are taken from Ref. [83]*

For PEMFCs operated at various loads, the required activities and mass transport rates are different because the reactant and product are nonuniformly distributed inside the membrane electrode assembly. Thus, a rational design for a membrane electrode assembly (MEA) with a spatial distribution of functional components helps reduce the usage of precious components, improve cell performance, and achieve uniform distributions of current density and heat. Thus, the graded design of the functional components in the GDL, MPL, CL, and membrane along both the through-plane and in-plane directions within the MEA were reviewed to reduce the cost and improve the performance and durability of proton exchange membrane fuel cells [84]. The simulation with a linear porosity gradient in the cathode GDL suggested remarkable improvement of the limiting current density and oxygen usage with an optimal linear porosity gradient with a porosity of 70% near the channel and 30% near the CL for the parallel and z-serpentine channel designs [85]. The results for the parallel channel are shown in Figure 3.4. It was found that the current density increases from 1.41 to 1.66 A cm^{-2} when the abovementioned graded porosity distribution was applied. The same trends are also observed for parallel and interdigitated channel designs. Weng et al. [86] designed a hydrophobicity-graded MPL and experimentally studied the cell performance under a variety of humidification conditions. Three MPLs with various PTFE contents, 20, 25, and 30 wt% in the MPLs from the CL/MPL interface to the MPL/GDL interface, were sandwiched between the CL and GDL. Thanks to the relatively low PTFE loading inside the inner layer of the as-prepared MPL, product water from the oxygen reduction reaction was retained within the CL under low humidity conditions, e.g., 5%. In contrast, the hydrophobicity-graded MPL efficiently discharged liquid water from the porous electrodes at high relative humidity, e.g., 50%, leading to improved cell performance, as shown in Figure 3.5. Srinivasarao et al. [87] developed a 2D and two-phase model to optimize Pt-loading, ionomer loading, the weight fraction of platinum on carbon, and CL thickness of a novel design with multiple CLs. They suggested that to achieve the same cell performance as that obtained from a single CL design, the overall loading of platinum should be reduced when a multilayer CL is applied. Moreover, the optimal Pt-loading of the CL close to the GDL was higher than that of the CL close to the membrane, as shown in Figure 3.6, in which CL1 represents the MPL-CL interface and CL4 corresponds to the CL-membrane interface. In the base case design, the Pt-loading was fixed at 0.25 mg cm^{-2} and uniformly distributed in different sublayers. At high cell voltages, the optimal platinum distribution almost does not change. At decreasing cell voltage, which corresponds to an increase in current density, the optimal Pt-loading decreases from the CL-membrane interface toward the MPL-CL interface. At 0.4 V, the optimal Pt-loading within the CL-membrane interface decreases to 0.15 mg cm^{-2}. This trend was confirmed by the work of Xing et al. [88].

For a function-graded PEM, a gradient density of sulfonic acid groups along the membrane thickness direction is typically used as the definition [89]. In most previous studies, such partially fluorinated sulfonic acid membranes (part-FSAs) were prepared using irradiation methods, e.g., a low-energy electron beam (EB) [90, 91]. The mechanism of improving the cell performance is the control of the membrane water uptake. Sato et al. [89] fabricated an FN (hybrid membrane) by mixing s-FEP (sulfonated radiation grafted membrane) powder with a Nafion dispersion and compared the water uptake, ion exchange capacity (IEC) and cell performance achieved by using FN, s-FEP and Nafion®112 as the membrane, respectively. The IEC and water uptake of the FN were improved compared to those of the Nafion®112 and s-FEP, resulting in the highest cell performance among the tested membranes, as shown in Figure 3.7. The design of GDL perforation also enhances the gas supply and water removal, which is discussed in Chapter 13.
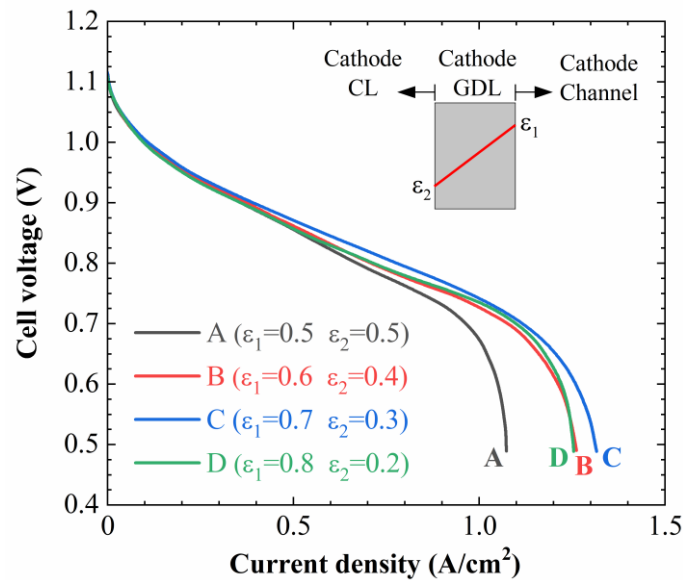

FIGURE 3.4 Predicted cell performance for a porosity-graded cathode GDL with parallel channel design. *Data are taken from Ref. [85].*
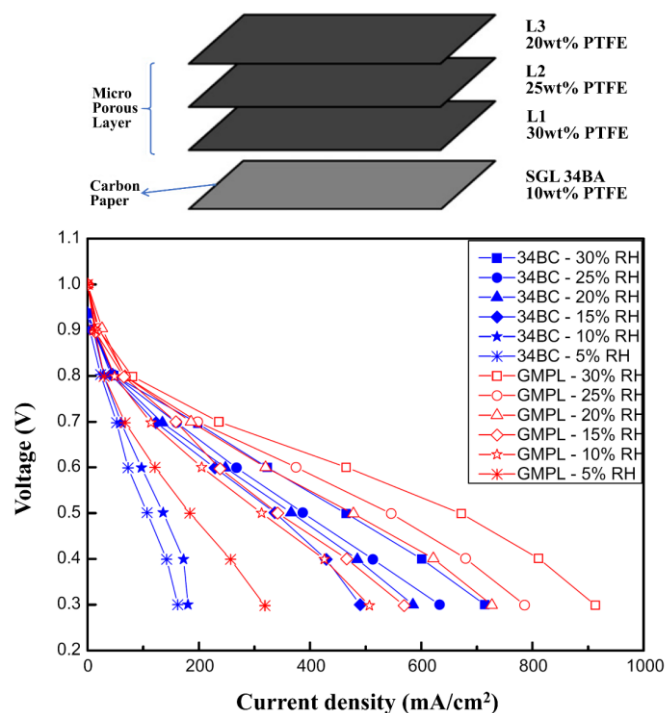
FIGURE 3.5 The cell performance of the commercial MPL (34BC) and GMPL under various relative humidity conditions: the GMPL consists of 34BA (10 wt% PTFE) and three sublayers with various PTFE loadings from 20 to 30 wt%. *Credit: Reprinted from Weng et al., International Journal of Hydrogen Energy, 36 (21), 13708–13714, 2011, with permission from Elsevier.*
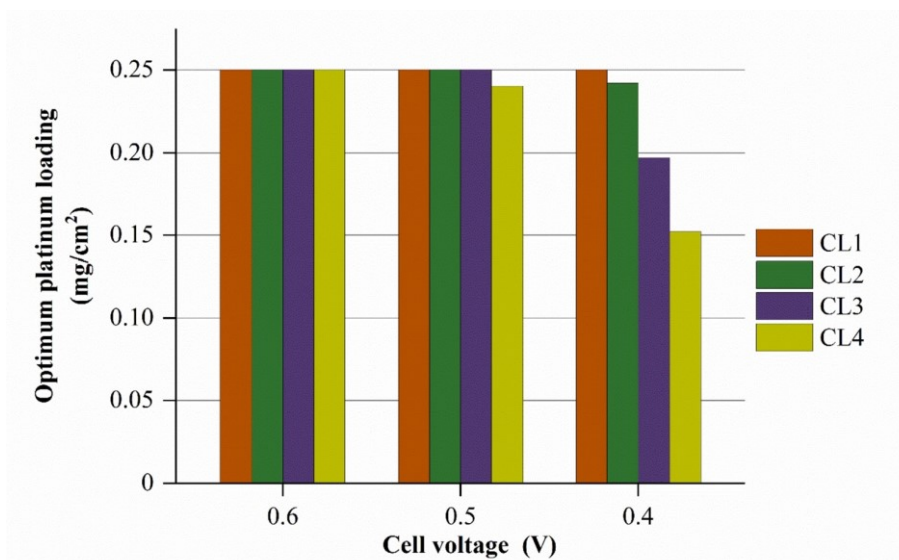

FIGURE 3.6 Optimum distribution of platinum loading in a multilayer CL at various cell voltages: CL1 is the sublayer close to the GDL, and CL4 is the sublayer close to the membrane. *Credit: Reprinted from Xing et al., Energy, 177 (15), 445–464, 2019, with permission from Elsevier.*
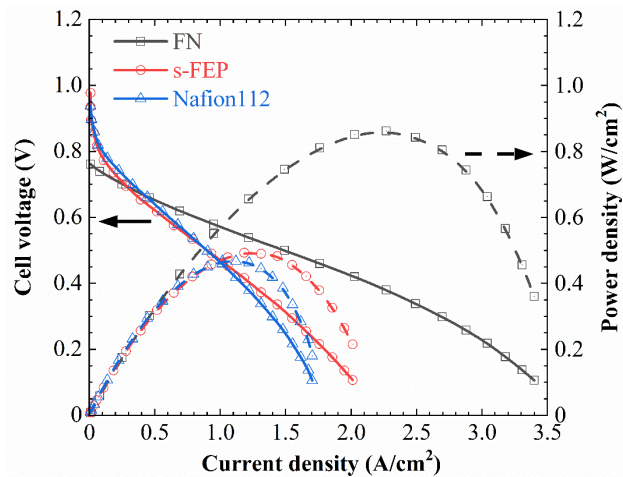
FIGURE 3.7 Cell performances of MEAs based on FN (mixture of the radiation-grafted membrane with Nafion ionomer), s-FEP (sulfonated radiation-grafted membrane) and Nafion® 112. Solid lines are for cell voltage, while dashed lines represent corresponding power densities. *Data are taken from Ref. [89].*

3.2 Flow fields optimization

The early efforts in the flow field design and optimization were published in 2004 [92]. The unique optimization objective was to maximize the current density at a cell voltage of 0.7 V with an interdigitated flow field. The design parameters included cathode pressure inlet, cathode GDL thickness, the width ratio of the gas channel and the current collector. However, all design variables reached the bounds of the optimal design. It was shown that the channel width ratio and the porosities of GDLs and CLs can be optimized using a gradient-based optimization algorithm (simplified conjugate gradient method)[93]. The optimal channel width ratio of 0.54, GDL porosity of 0.6, and CL porosity of 0.3 were obtained in the optimization results.

To maintain sufficient reactant supply, excellent water removal, and low pressure drop, various novel flow field designs, in addition to traditional parallel, interdigitate, and serpentine design, have been proposed and studied [94-101]. For instance, a porous-blocked baffled flow channel was designed [94], in which porous blocks were installed between GDL and baffles. A two-phase, non-isothermal model was developed to investigate the mass transport mechanisms and optimize the porosities of the blocks at different locations along the channel for improved cell performance and reduced pumping power. In their later work [95], the baffled channel with three different leeward lengths along the flow field channels was designed and the pumping power, net power, and power density were experimentally studied. A most recent modeling work on the combination of baffles and a secondary porous layer includes the complete formulation of the Forchheimer inertial effect [96]. The porous and baffled flow field improved the cell performance by minimizing mass transport losses, and enhancing water removal from the GDL. The metal-foam and honeycomb flow fields were also employed to facilitate the water

management and reactant transport within the porous electrode and to achieve higher uniformities of reactant and current distributions than the traditional parallel straight flow field [97, 98]. To improve the water removal and cell performance, a series of sub-inlet at the parallel cathode flow channels was introduced [99, 102], and was found that a suitable location of the sub-inlet along the channel and a reasonable amount of dry air fed from the sub-inlet could benefit water removal and cell performance with a small pressure along the channel. Novel confrontational design of flow fields is only important when considerable liquid water was generated at medium and high current densities, as different configurations of flow fields have very limited influence on the cell performance at low current densities [103-105].

In the past, different shapes of flow fields named by alphabet letters, such as S-shaped [100], M-like [101], and Z-shaped [106] flow fields have been applied to promote the overall performance of fuel cells through the enhancement of mass transport and water removal. As shown in Figure 3.8, a novel flow field was designed recently by deploying auxiliary channels inside the partially hollow ribs and drilling a series of arrayed holes on the auxiliary channels [107]. This novel design rationally utilizes the ribs of the current collector and improves the volumetric efficiency of the parallel channels, leading to improved cell performance and homogeneity of current distribution. It showed that an optimization of the flow field geometry, i.e., the hole size, the area ratio of arrayed holes and auxiliary channels, nonuniform distribution of arrayed holes, could further improve the cell performance and current uniformity at an extremely lower pressure-drop. Commercialized flow fields, such as the 3D fine-mesh design used in Toyota Mirai [108, 109] and the wave-like flow fields implemented in Honda Clarity [110] are promising solutions regarding the liquid water removal from the cell at high current density. In addition, bio-inspired flow fields, such as tree-shaped [111] and lung-shaped [112] flow fields are commendable attempts to redistribute the reactant gas and improve the forced convection. The mass transfer in the novel flow fields is discussed in detail in Chapter 13.
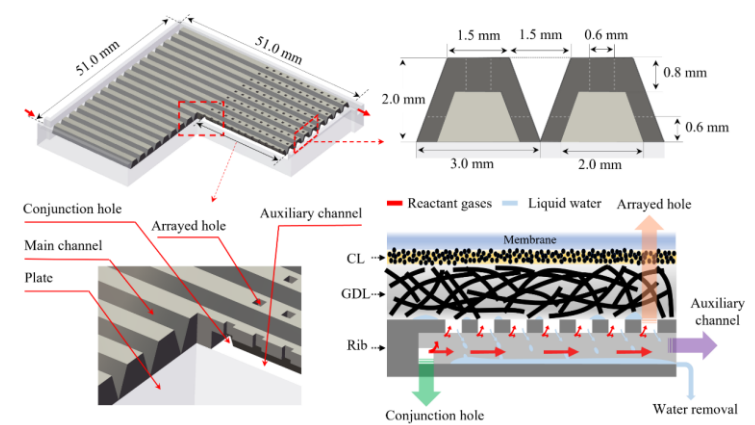

FIGURE 3.8 A novel flow field design with auxiliary channels and arrayed holes. *Credit: Reprinted from Wang et al., AIChE Journal, 68 (2), e17461, 2022, with permission from John Wiley and Sons.*

The modification of channel geometry and installation of obstacles in the channel is to increase the gas velocity near the outlet region and change the laminar gas flow to a turbulent pattern, with the aim of enhancing the mass transport through the porous electrodes. However, these tapered channels and baffle channels suffer from technical difficulties in the manufacture and significant pressure drop. In addition, the precious control of the pressure difference between adjacent channels is a great challenge in these configurations. Thus, a promising solution is to modify the simple parallel field to create a reasonable pressure difference between the adjacent parallel channels, for better water drainage, more efficient utilization of the rib area, and more uniform current distribution. An easily machined novel flow field with a controllable pressure gradient across adjacent channels was manufactured and numerically studied by a 2D two-phase flow model. The effect of channel-rib width ratio, GDL thickness, and pressure gradient on the profiles of oxygen concentration and water saturation within the electrode were investigated [113].

3.3 Fuel cell stack optimization

Fuel cell stack optimization has received little attention compared with flow field design, electrode design, and operating condition optimization. In the fuel cell stack, the clamping load applied to a PEMFC stack is considered the most important effect on fuel cell performance due to the influence on electron transfer, mass, and thermal transport [114]. The modeling results showed that an optimal compression deformation exists when the contact resistance was considered [115]. Mohamed and Jenkins [116] optimized the number of cells in series based on a simplified zero-dimensional, isothermal fuel cell stack model, in which the optimization objective was to maximize the power output. Zhou et al. [117] developed a cold start model for PEMFCs aimed at optimizing the start-up methods. As a novel method, variable heating and load control (VHLC) was proposed.

A notable feature of vehicular PEMFCs is that the fuel cell stack must undergo frequent start-up and shut-down (SU/SD) processes, which is considered one of the main mechanisms of fuel cell durability degradation [118]. Before the start of PEMFC stacks, the anode flow channel is filled with air. When hydrogen enters the anode, a process of replacing air with hydrogen is required, leading to the formation of a hydrogen/air interface at the anode side. The formation of the hydrogen-air interface results in extremely high electrode potential in the cathode catalyst layer, which leads to the oxygen evolution reaction and carbon corrosion reaction. It is named the reverse current decay mechanism, which is widely accepted as the basis for the degradation of PEMFC stacks during SU/SD processes. Since reactant gases remain in the fuel cell stack after the SD process, the potential between the electrode and proton-exchange-membrane

19

generated in the SU process would cause considerable degradation of fuel cell stack components, e.g., carbon corrosion, leading to a significant reduction of PEMFC life.

To optimize the operation of fuel cell stacks and mitigate the degradation in SU/SD processes, two strategies, gas purge, and auxiliary load, are commonly applied [119, 120]. The gas purge normally uses inert gases, e.g., nitrogen, to purge reactant gases out of the stack, which could effectively reduce the residence time of reactant gases within the fuel cell stacks, achieving a relatively low potential between the CL and the proton-exchange-membrane [121]. Different gas purge strategies are sometimes combined, for example, using the anode reactant as the purge gas at the cathode, and vice versa. Oyarce et al. [122] compared four different gas purge strategies and found that the lifetime of PEMFCs was significantly improved. Although nitrogen purge is the most effective strategy, the availability of nitrogen limits the application of this strategy in practical PEMFCs. For the auxiliary load strategy, an extra load is applied on the fuel cell stack to consume the residual reactant gases in the porous electrodes. Thus, the potential difference between the CL and membrane is limited to a safe range to alleviate the degradation and improve the durability of the fuel cell stack. For example, the application of a higher dummy load could eliminate the high potential at the cathode more promptly during the SD process [123]. The results of Yang et al. [124] showed that the auxiliary load can effectively shorten the duration time of the hydrogen/air interface during the SD process, thereby eliminating the generation of reverse current. However, the implementation of an auxiliary load may cause local gas starvation, which could be avoided by the air purge. As a result, the hybrid strategy, which combines auxiliary load and air purge, is considered a more effective way to mitigate fuel cell stack degradation [125].

3.4 Operating condition optimization

The improved cell performance can be achieved with higher operating temperature, inlet pressure, and stoichiometric flow ratio due to lower activation and ohmic overpotentials [73, 126-128]. Consequently, both an accurate fuel cell model and a complete fuel cell system model must be coupled in the optimization of operating conditions. Otherwise, the optimization algorithm would always choose the higher values of the operating parameters [129]. The early efforts in the optimization of the operating conditions can be found in 2000 [130]. The objective was to maximize the power density at a fixed current density. The design variables included operating temperature, pressures of anode and cathode, mole fractions of the gas inlet, stoichiometry, and relative humidity. Minimizing membrane hydration, maximizing temperature rise and cell voltage were the additional constraints. The optimization results indicated that the optimal operating conditions strongly depend on the current densities. Wu et al. [131] optimized the efficiency of the fuel cell system at low, medium, and high current densities. The design variables used were the operating temperature, pressure of cathode gas

inlet, stoichiometry, and relative humidity. The optimization results suggested that, for a realistic system, the optimal cathode stoichiometry was between 1.25 and 2, cathode pressure between 1.5 and 3 atm, and cathode relative humidity between 10% and 15%. Xing et al. [132] optimized the cathode relative humidity for different Nafion® ionomer content inside the cathode CL by a 2D, isothermal, two-phase flow model. The optimal ionomer content of 10% was found for fully humidified inlet gas at the cathode. The optimal relative humidity was between 73% to 85% when the ionomer volume fraction was in the range of 10% to 50%. The operating conditions were also supervised and optimized through a data-driven surrogate model [133].

3.5 Multi-variable optimization and data-driven surrogate modeling

Since the optimal graded distributions of different components are simultaneously preceded in parallel, e.g., the design of both a graded GDL and a graded MPL [134], multi-variable optimization is an efficient method by which to optimize the cell performance by simultaneously optimizing a variety of variables. For example, Secanell et al. optimized both the Pt-loading and the performance of a complete MEA [82, 135]. The design variables included Pt-loading, ionomer loading, GDL porosity and hydrophilicity, and platinum-to-carbon mass ratio. It was shown that the cell performance was significantly improved by using the parameters obtained from the optimal design. The optimization results suggested that the cell performance can be improved by increasing the ionomer content and reducing the catalyst loadings. In addition, the Pt-loading had to be controlled within the range of 0.1-0.5 mg cm^{-2}, as higher loadings resulted in the waste of platinum rather than an increase in current density. A two-objective function multivariable optimization of the cathode composition of the PEMFC was carried out by Xing et al. [136]. Five design variables, including the Pt-loading, Pt/C ratio, ionomer volume fraction, CL thickness, and agglomerate size, were optimized through multiple surrogate models, and their sensitivities were analyzed by a Monte Carlo method-based approach. As a novel optimization strategy, maximizing the current density within a specific range of cell voltages was implemented for the prediction of the optimum values. In their later work, the interaction of graded Pt-loading and GDL porosity [137], Pt-loading and operating temperature [138], along the in-plane direction were numerically studied to reduce the usage of Pt-based catalyst and improve the cell performance and current homogeneity.

An optimization problem involving D objectives and K constraints can be formulated as:

$$\underset{x}{\text{minimize}}\ Y(x) = \{y_1(x), y_2(x), \cdots, y_D(x)\}$$

$$subject\ to\ G(x) = \{g_1(x), g_2(x), \cdots, g_K(x)\} \tag{3-7}$$

$$\text{and } \boldsymbol{x} = (x_1, x_2, \cdots, x_n,)^T \in \prod_{i=1}^{n} [l_i, u_i]$$

where Y is the objectives and G is the constraints of the optimization design. n is the number of design variables, and $-\infty < l_i < u_i < +\infty$ for all $i = 1, 2, \cdots, n$. $\prod_{i=1}^{n} [l_i, u_i]$ means the range of the design variables, terms as the design space. The basic process of an optimization design is shown in Figure 3.9.
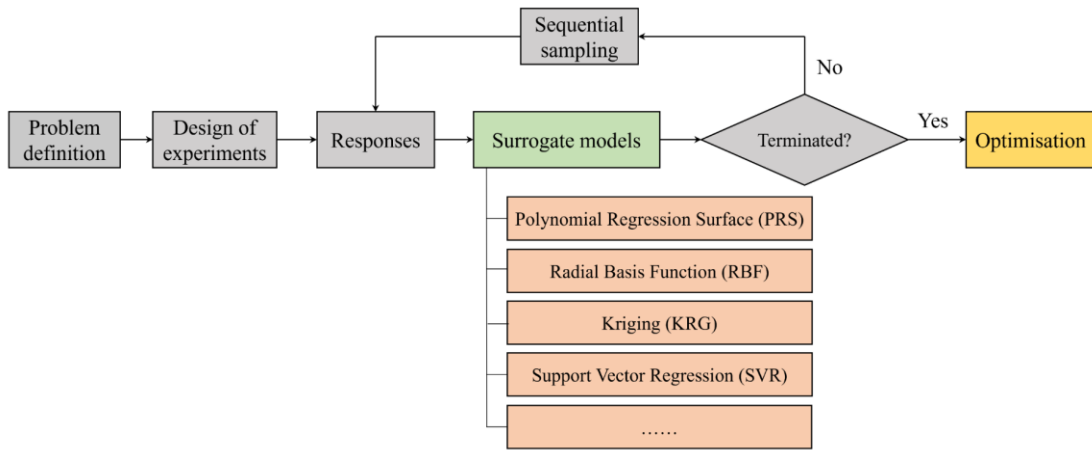

FIGURE 3.9 A typical process of optimization design.

The data-driven optimization design is started with the definition of the problem, including the design variables and their ranges, the objectives, and the constraints. According to the formulated design problem, the design of experiments (DoE) is employed to generate the initial samples in the design space, and the response of each sample is obtained by a corresponding run of simulation or experiment. Then, the unknown mapping relationship between the input variables and their output responses is approximated using the surrogate model, which plays an important role in the optimization design and has a significant impact on the optimization results. Therefore, the accuracies of the surrogate models are calculated to determine whether the model can be used for the following optimization design. If the model accuracy can not satisfy the optimization requirements, new samples will be obtained by sequential sampling algorithms to improve the surrogate model until the model accuracy or computational cost met the termination conditions.

Although time and resources could be significantly reduced through the use of complex physical models, e. g., the multi-physics and multi-phase flow models, the computational and time costs are still unaffordable when solving partial differential equations (PDEs) over complex geometry, e. g. few days or weeks are required to solve a 3D steady-state small fuel

cell stack model discretized into less than 100 million nodes of grid[139-141]. In this regard, a feasible approach is to train the machine learning and AI model with a certain number of data obtained from the complex mechanistic physical models, which typically refer to data-driven surrogate modeling, as shown in Figure 3.10. Data-driven surrogate models have been applied to predict PEMFC performance in steady-state and dynamic conditions [133, 142], screen catalyst materials [143, 144], optimize electrode composition [145, 146], and assist the development of control strategies to maximize the cell performance and mitigate material degradation [147, 148].
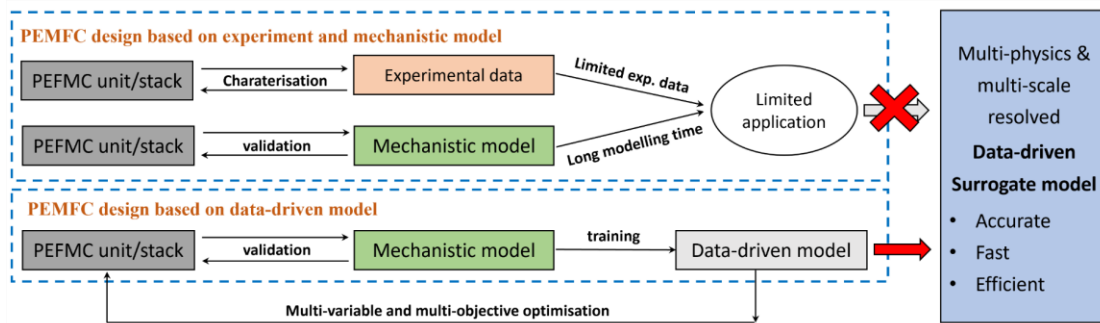

FIGURE 3.10 An illustrative flowchart of PEMFC unit/stack design based on data-driven surrogate modeling.

There are numerous published works optimizing the PEMFC's performance through the implementation of data-driven surrogate models. For example, Lan et al. [149] optimized the stoichiometric ratio and flow channel geometry for high-temperature proton exchange membrane (HT-PEM) fuel cells based on artificial neural networks (ANN) to reduce the high computational cost of experiments or simulations. A few samples with representative performance information of fuel cells were used for approximating the complex mapping relationship between different designs with the stoichiometric ratio and flow channel geometry. The flow channel geometry was optimized for maximum current density and maximum real power under a fixed operating cell voltage. Wang et al. [150] integrated a three-dimensional CFD fuel cell model with an AI-based data-driven surrogate model and an optimization framework to realize the multi-variable global optimization of CL composition for improving the maximum power density. Support vector machine (SVM) machine learning model was trained by the data obtained from the physical model then a genetic algorithm (GA) was employed to search the optimal values of voltage, Pt-loading, Pt percentage, IC ratio, volume fractions of ionomer, and pores. Ding et al. [151] built a data-driven surrogate model to optimize the catalyst loading and ionomer content to improve Pt utilization. In their work, eight machine learning algorithms were compared, and ANN achieved the best prediction accuracy. It is widely accepted that a comprehensive physical model, after experimental validation, lays

the foundation of a data-driven surrogate model because the data used for machine learning model training is the output of the physical model. Thus, the more processes that could be taken into account in a physical model, the higher reliability of the generated database for machine learning model training.

4. Summary

In this chapter, the chronological development of PEMFC modeling approaches is introduced, the models built at different times are compared, and key physicochemical and operating parameters are discussed. As an important process occurred during the operation of PEMFCs, particular attention is paid to the modeling approaches for water formation and transport through the membrane and the porous electrode. Different approaches to CL digitalization are also discussed and compared. In the past thirty years, a large number of numerical models have been developed, which were chronologically developed by adding complexities and details to existing simple models. These models were developed from single-physics to multi-physics, from 1D to 3D, from single-phase flow to two-phase flow, and from isothermal to non-isothermal. The computational domain has also been significantly expanded from a single cell unit to multi-cell fuel-cell stacks consisting of a series of single cells.

Numerical modeling is important to the diagnosis, design, optimization, and development of novel PEMFCs because the need for experimental resources and time is greatly reduced. Experimentally-validated sophisticated numerical models could be used to optimize the PEMFC's electrodes, flow fields, fuel cell stack, and operating conditions. The endeavor of PEMFC optimization has been proven to be an effective way to achieve better water management, more uniform reactants distributions, reinforced mass transport, and prolonged fuel cell life. The latest development of data-driven surrogate modeling attracts increasing attention owing to reduced computational time which is offered by mechanistic multi-physics and multi-phase flow PEMFC models. A feasible approach is to train the machine learning and AI models with limited training data obtained from sophisticated mechanistic models. Then use the data-driven surrogate model to predict the cell performance instead of the mechanistic model. In recent years, AI-based data-driven surrogate modeling has been successfully implemented in PEMFC optimization, which can be a promising approach in the future.

References

[1] A. Weber, R. Borup, R. Darling, P.K. Das, T. Dursch, W. Gu, D. Harvey, A. Kusoglu, S. Litster, M.M. Mench, R. Mukundan, J. Owejan, J.G. Pharoah, M. Secanell, I. Zenyuk, Journal of The Electrochemical Society, 161 (2014) F1254-F1299.
[2] V. Gurau, H. Liu, S. Kakaç, AIChE Journal, 44 (1998) 2410-2422.
[3] T. Hottinen, O. Himanen, Electrochemistry Communications, 9 (2009) 1047-1052.
[4] W.M. Yan, C. Soong, F. Chen, H.S. Chu, Journal of Power Sources, 125 (2004) 27-39.

[5] L. Xing, Y. Xu, P.K. Das, B. Mao, Q. Xu, H. Su, X. Wu, W. Shi, Chemical Engineering Science, 195 (2019) 127-140.

[6] M. Kawase, K. Sato, R. Mitsui, H. Asonuma, M. Kageyama, K. Yamaguchi, G. Inoue, AIChE Journal, 63 (2017) 249-256.

[7] T. Van Nguyen, M.W. Knobbe, Journal of Power Sources, 114 (2003) 70-79.

[8] M.A. Hickner, C.H. Fujimoto, C.J. Cornelius, Polymer, 47 (2006) 4238-4244.

[9] J. Stumper, M. Löhr, S. Hamada, Journal of Power Sources, 143 (2005) 150-157.

[10] H. Meng, C.-Y. Wang, Journal of The Electrochemical Society, 152 (2005) A1733-A1741.

[11] G. Janssen, M.L.J. Overvelde, Journal of Power Sources, 101 (2001) 117-125.

[12] S. Knights, K. Colbow, J. St-Pierre, D. Wilkinson, Journal of Power Sources, 127 (2004) 127-134.

[13] C.-Y. Wang, P. Sinha, ECS Transactions, 3 (2006) 387-396.

[14] E. Kumbur, K. Sharp, M.M. Mench, Journal of The Electrochemical Society, 154 (2007) B1315-B1324.

[15] D. Natarajan, T. Van Nguyen, Journal of The Electrochemical Society, 148 (2001) A1324-A1335.

[16] P. Berg, K. Promislow, J. St. Pierre, J.r. Stumper, B. Wetton, Journal of The Electrochemical Society, 151 (2004) A341-A353.

[17] U. Pasaogullari, C.Y. Wang, Journal of The Electrochemical Society 151 (2004) A399-406.

[18] P.K. Das, X. Li, Z.-S. Liu, International Journal of Hydrogen Energy, 35 (2010) 2403-2416.

[19] T.E. Springer, T. Zawodzinski, S. Gottesfeld, J. Electrochem. Soc., 138 (1991) 2334-2342.

[20] T.E. Springer, M.S. Wilson, S. Gottesfeld, Journal of The Electrochemical Society, 140 (1993) 3513-3526.

[21] D.M. Bernardi, M.W. Verbrugge, Journal of The Electrochemical Society, 139 (1992) 2477-2491.

[22] D.M. Bernardi, M.W. Verbrugge, AIChE Journal, 37 (1991) 1151-1163.

[23] T.V. Nguyen, R.E. White, Journal of The Electrochemical Society, 140 (1993) 2178-2186.

[24] T.F. Fuller, J. Newman, Journal of The Electrochemical Society, 140 (1993) 1218-1225.

[25] J.S. Yi, T.V. Nguyen, Journal of The Electrochemical Society, 145 (1998) 1149-1159.

[26] J.S. Yi, T. Van Nguyen, Journal of The Electrochemical Society, 146 (1999) 38-45.

[27] F. Gloaguen, R. Durand, Journal of Applied Electrochemistry, 27 (1997) 1029-1035.

[28] Y. Bultel, P. Ozil, R. Durand, Journal of Applied Electrochemistry, 28 (1998) 269-276.

[29] Y. Bultel, P. Ozil, R. Durand, Electrochimica Acta, 43 (1998) 1077-1087.

[30] Y. Bultel, P. Ozil, R. Durand, Journal of Applied Electrochemistry, 29 (1999) 1025-1033.

[31] C. Marr, X. Li, Journal of Power Sources, 77 (1999) 17-27.

[32] D. Spernjak, A.K. Prasad, S.G. Advani, Journal of Power Sources, 170 (2007) 334-344.

[33] K. Tüber, D. Pócza, C. Hebling, Journal of Power Sources, 124 (2003) 403-414.

[34] S. Dutta, S. Shimpalee, J.W. Van Zee, Journal of Applied Electrochemistry, 30 (2000) 135-146.

[35] S. Dutta, S. Shimpalee, J.W. Van Zee, International Journal of Heat and Mass Transfer, 44 (2001) 2029-2042.

[36] T. Zhou, H. Liu, Int. J. Transp. Phenom., 3 (2001) 177-198.

[37] T. Berning, D.M. Lu, N. Djilali, Journal of Power Sources, 106 (2002) 284-294.

[38] S. Mazumder, J.V. Cole, Journal of The Electrochemical Society, 150 (2003) A1503.

[39] S. Mazumder, J.V. Cole, Journal of The Electrochemical Society, 150 (2003) A1510-A1517.

[40] W.k. Lee, S. Shimpalee, J.W. Van Zee, Journal of The Electrochemical Society, 150 (2003) A341.

[41] S. Um, C.Y. Wang, Journal of Power Sources, 125 (2004) 40-51.

[42] Y. Wang, C.-Y. Wang, Electrochimica Acta, 50 (2005) 1307-1315.
[43] B.S. Machado, N. Chakraborty, P.K. Das, International Journal of Hydrogen Energy, 42 (2017) 6310-6323.
[44] B.S. Machado, N. Chakraborty, M. Mamlouk, P.K. Das, Journal of Electrochemical Energy Conversion and Storage, 15 (2018) 011004.
[45] Z. Liu, Z. Mao, C. Wang, W. Zhuge, Y. Zhang, Journal of Power Sources, 160 (2006) 1111-1121.
[46] S. Shimpalee, S. Greenway, D. Spuckler, J.W. Van Zee, Journal of Power Sources, 135 (2004) 79-87.
[47] H. Ju, H. Meng, C.-Y. Wang, International Journal of Heat and Mass Transfer, 48 (2005) 1303-1315.
[48] Y. Wang, C.-Y. Wang, Journal of Power Sources, 153 (2006) 130-135.
[49] W. He, J.S. Yi, T. Van Nguyen, AIChE Journal, 46 (2000) 2053-2064.
[50] D. Natarajan, T. Van Nguyen, Journal of Power Sources, 115 (2003) 66-80.
[51] T. Berning, N. Djilali, Journal of The Electrochemical Society, 150 (2003) A1589.
[52] G. Lin, T.V. Nguyen, Journal of The Electrochemical Society, 153 (2006) A372.
[53] Q. Ye, T.V. Nguyen, Journal of The Electrochemical Society, 154 (2007) B1242.
[54] P.C. Sui, S. Kumar, N. Djilali, Journal of Power Sources, 180 (2008) 410-422.
[55] Y. Wang, S. Basu, C.-Y. Wang, Journal of Power Sources, 179 (2008) 603-617.
[56] P. Quan, B. Zhou, A. Sobiesiak, Z. Liu, Journal of Power Sources, 152 (2005) 131-145.
[57] B. Xie, G. Zhang, Y. Jiang, R. Wang, X. Sheng, F. Xi, Z. Zhao, W. Chen, Y. Zhu, Y. Wang, H. Wang, K. Jiao, eTransportation, 6 (2020) 100090.
[58] B. Xie, M. Ni, G. Zhang, X. Sheng, H. Tang, Y. Xu, G. Zhai, K. Jiao, International Journal of Heat and Mass Transfer, 189 (2022) 122705.
[59] J.S. Newman, Electrochemical systems, 2nd edition, Prentice Hall, 1991.
[60] P.N. Pintauro, D.N. Bennion, Industrial & Engineering Chemistry Fundamentals, 23 (1984) 230-234.
[61] A.Z. Weber, J. Newman, Journal of The Electrochemical Society, 150 (2003) A1008-A1015.
[62] J.H. Nam, M. Kaviany, International Journal of Heat and Mass Transfer, 46 (2003) 4595-4611.
[63] W. Sun, B.A. Peppley, K. Karan, Electrochimica Acta, 50 (2005) 3359-3374.
[64] P.K. Das, X. Li, Z.-S. Liu, Journal of Power Sources, 179 (2008) 186-199.
[65] Y. Wang, C.-Y. Wang, Electrochimica Acta, 51 (2006) 3924-3933.
[66] S. Basu, J. Li, C.-Y. Wang, Journal of Power Sources, 187 (2009) 431-443.
[67] J.W. Park, K. Jiao, X. Li, Applied Energy, 87 (2010) 2180-2186.
[68] Y.B. Salah, Y. Tabe, T. Chikahisa, Energy Procedia, 28 (2012) 125-133.
[69] L.-P. Wang, B. Afsharpoya, Mathematics and Computers in Simulation, 72 (2006) 242-248.
[70] J. Park, M. Matsubara, X. Li, Journal of Power Sources, 173 (2007) 404-414.
[71] Y. Gao, X.X. Zhang, P. Rama, Y. Liu, R. Chen, H. Ostadi, K. Jiang, Fuel Cells, 12 (2012) 365-381.
[72] K.T. Jeng, S.F. Lee, G.F. Tsai, C.H. Wang, Journal of Power Sources, 138 (2004) 41-50.
[73] P.K. Das, X. Li, Z.-S. Liu, Journal of Electroanalytical Chemistry, 604 (2007) 72-90.
[74] L. Xing, M. Mamlouk, K. Scott, Energy, 61 (2013) 196-210.
[75] L. Xing, M. Mamlouk, R. Kumar, K. Scott, International Journal of Hydrogen Energy, 39 (2014) 9087-9104.
[76] L. Xing, Q. Cai, C. Xu, C. Liu, K. Scott, Y. Yan, Energy, 106 (2016) 631-645.
[77] L. Xing, Q. Cai, X. Liu, C. Liu, K. Scott, Y. Yan, Chemical Engineering Science, 146 (2016) 88-103.
[78] L. Xing, Chemical Engineering Science, 179 (2018) 198-213.
[79] P.K. Das, X. Li, Z. Xie, Z.-S. Liu, International Journal of Energy Research, 35 (2011) 1325-1339.
[80] D. Song, Q. Wang, Z. Liu, T. Navessin, M. Eikerling, S. Holdcroft, Journal of Power Sources, 126 (2004) 104-111.

[81] D. Song, Q. Wang, Z. Liu, T. Navessin, S. Holdcroft, Electrochimica Acta, 50 (2004) 731-737.

[82] M. Secanell, R. Songprakorp, A. Suleman, N. Djilali, Energy & Environmental Science, 1 (2008) 378-388.

[83] M. Secanell, K. Karan, A. Suleman, N. Djilali, Electrochimica Acta, 52 (2007) 6318-6337.

[84] L. Xing, W. Shi, H. Su, Q. Xu, P.K. Das, B. Mao, K. Scott, Energy, 177 (2019) 445-464.

[85] Y.-X. Huang, C.-H. Cheng, X.-D. Wang, J.-Y. Jang, Energy, 35 (2010) 4786-4794.

[86] F.-B. Weng, C.-Y. Hsu, M.-C. Su, International Journal of Hydrogen Energy, 36 (2011) 13708-13714.

[87] M. Srinivasarao, D. Bhattacharyya, R. Rengaswamy, Journal of Power Sources, 206 (2012) 197-203.

[88] L. Xing, W. Shi, P.K. Das, K. Scott, AIChE Journal, 63 (2017) 4895-4910.

[89] Y. Sato, K. Fujii, N. Mitani, A. Matsuura, T. Kakigi, F. Muto, J. Li, A. Oshima, M. Washio, Nuclear Instruments and Methods in Physics Research Section B: Beam Interactions with Materials and Atoms, 265 (2007) 213-216.

[90] H. Fujita, F. Shiraki, Y. Oshima, T. Tatsumi, T. Yoshikawa, T. Sasaki, A. Oshima, M. Washio, Radiation Physics and Chemistry, 80 (2011) 201-206.

[91] H. Fujita, F. Shiraki, T. Yoshikawa, A. Oshima, M. Washio, Journal of Photopolymer Science and Technology, 23 (2010) 387-392.

[92] M. Grujicic, K.M. Chittajallu, Applied Surface Science, 227 (2004) 56-72.

[93] H.-H. Lin, C.-H. Cheng, C.-Y. Soong, F. Chen, W.-M. Yan, Journal of Power Sources, 162 (2006) 246-254.

[94] H. Chen, H. Guo, F. Ye, C.F. Ma, Q. Liao, X. Zhu, International Journal of Energy Research, 43 (2019) 2910-2929.

[95] H. Chen, H. Guo, F. Ye, C.F. Ma, Journal of Power Sources, 472 (2020) 228456.

[96] L. Mihanović, Ž. Penga, V. Hacker, Energies, 14 (2021) 3675.

[97] Z. Bao, Z. Niu, K. Jiao, International Journal of Hydrogen Energy, 44 (2019) 6229-6244.

[98] S.A. Atyabi, E. Afshari, Journal of Cleaner Production, 214 (2019) 738-748.

[99] Y. Wang, L. Yue, S. Wang, Journal of Power Sources, 344 (2017) 32-38.

[100] L. He, M. Hou, Y. Gao, X. Sun, W. Song, L. Zheng, J. Ai, H. Zhang, Z. Shao, Energy Conversion and Management, 223 (2020) 113292.

[101] C. Yang, Z. Wan, X. Chen, X. Kong, J. Zhang, T. Huang, X. Wang, Energy Conversion and Management, 228 (2021) 113651.

[102] Y. Wang, H. Xu, X. Wang, Y. Gao, X. Su, Y. Qin, L. Xing, Energy Conversion and Management, 252 (2022) 115069.

[103] X.-D. Wang, Y.-Y. Duan, W.-M. Yan, X.-F. Peng, Electrochimica Acta, 53 (2008) 5334-5343.

[104] X.-D. Wang, Y.-Y. Duan, W.-M. Yan, Journal of Power Sources, 173 (2007) 210-221.

[105] W.-M. Yan, H.-Y. Li, P.-C. Chiu, X.-D. Wang, Journal of Power Sources, 178 (2008) 174-180.

[106] M.K. Vijayakrishnan, K. Palaniswamy, J. Ramasamy, T. Kumaresan, K. Manoharan, T.K. Raj Rajagopal, T. Maiyalagan, V.R. Jothi, S.-C. Yi, International Journal of Hydrogen Energy, 45 (2020) 7848-7862.

[107] Y. Wang, X. Wang, G. Chen, C. Chen, X. Wang, Ž. Penga, Z. Yang, L. Xing, AIChE Journal, 68 (2022) e17461.

[108] T. Yoshida, K. Kojima, The Electrochemical Society Interface, 24 (2015) 45-49.

[109] J. Kim, G. Luo, C.-Y. Wang, Journal of Power Sources, 365 (2017) 419-429.

[110] M. Matsunaga, T. Fukushima, K. Ojima, World Electric Vehicle Journal, 3 (2009).

[111] C.E. Damian-Ascencio, A. Saldaña-Robles, A. Hernandez-Guerrero, S. Cano-Andrade, Energy, 133 (2017) 306-316.

[112] P. Trogadas, J.I.S. Cho, T.P. Neville, J. Marquis, B. Wu, D.J.L. Brett, M.O. Coppens, Energy & Environmental Science, 11 (2018) 136-143.

[113] L. Xing, Y. Xu, Ž. Penga, Q. Xu, H. Su, W. Shi, F. Barbir, AIChE Journal, 66 (2020) e16957.

[114] W. Zhang, C.W. Wu, Journal of Fuel Cell Science and Technology, 11 (2013) 020000.
[115] P. Zhou, C.W. Wu, Journal of Power Sources, 170 (2007) 93-100.
[116] I. Mohamed, N. Jenkins, Journal of Power Sources, 131 (2004) 142-146.
[117] Y. Zhou, Y. Luo, S. Yu, K. Jiao, Journal of Power Sources, 247 (2014) 738-748.
[118] K. Ettihir, L. Boulon, K. Agbossou, Applied Energy, 163 (2016) 142-153.
[119] R. Lin, X. Cui, J. Shan, L. Técher, F. Xiong, Q. Zhang, International Journal of Hydrogen Energy, 40 (2015) 14952-14962.
[120] Y.-T. Mu, P. He, J. Ding, L. Chen, W.-Q. Tao, Energy Procedia, 105 (2017) 1967-1973.
[121] Q. Shen, M. Hou, D. Liang, Z. Zhou, X. Li, Z. Shao, B. Yi, Journal of Power Sources, 189 (2009) 1114-1119.
[122] A. Oyarce, E. Zakrisson, M. Ivity, C. Lagergren, A.B. Ofstad, A. Bodén, G. Lindbergh, Journal of Power Sources, 254 (2014) 232-240.
[123] Y. Yu, X.-Z. Yuan, H. Li, E. Gu, H. Wang, G. Wang, M. Pan, International Journal of Hydrogen Energy, 37 (2012) 15288-15300.
[124] Y. Yang, W. Li, R. Lin, S. Xia, Z. Jiang, Journal of Power Sources, 404 (2018) 126-134.
[125] R. Lin, D. Liu, S. Xia, T. Ma, B. Dutruel, International Journal of Hydrogen Energy, 45 (2020) 1030-1044.
[126] A. Kazim, P. Forges, H.T. Liu, International Journal of Energy Research, 27 (2003) 401-414.
[127] S. Kim, S. Shimpalee, J.W. Van Zee, Journal of Power Sources, 135 (2004) 110-121.
[128] M. Amirinejad, S. Rowshanzamir, M.H. Eikani, Journal of Power Sources, 161 (2006) 872-875.
[129] J. Wishart, Z. Dong, M. Secanell, Journal of Power Sources, 161 (2006) 1041-1055.
[130] A. Mawardi, F. Yang, R. Pitchumani, Journal of Fuel Cell Science and Technology, 2 (2005).
[131] J. Wu, Q. Liu, H. Fang, Journal of Power Sources, 156 (2006) 388-399.
[132] L. Xing, P.K. Das, X. Song, M. Mamlouk, K. Scott, Applied Energy, 138 (2015) 242-257.
[133] B. Wang, G. Zhang, H. Wang, J. Xuan, K. Jiao, Energy and AI, 1 (2020) 100004.
[134] A.M. Kannan, L. Cindrella, L. Munukutla, Electrochimica Acta, 53 (2008) 2416-2422.
[135] M. Secanell, R. Songprakorp, N. Djilali, A. Suleman, Structural and Multidisciplinary Optimization, 40 (2009) 563.
[136] L. Xing, X. Song, K. Scott, V. Pickert, W. Cao, International Journal of Hydrogen Energy, 38 (2013) 14295-14313.
[137] L. Xing, Y. Wang, P.K. Das, K. Scott, W. Shi, Chemical Engineering Science, 192 (2018) 699-713.
[138] L. Xing, Y. Xu, Ž. Penga, Q. Xu, H. Su, F. Barbir, W. Shi, J. Xuan, Chemical Engineering Journal, 406 (2021) 126889.
[139] G.-H. Song, H. Meng, Acta Mechanica Sinica, 29 (2013) 318-334.
[140] A. Demuren, R. Edwards, Modeling Proton Exchange Membrane Fuel Cells—A Review, in, 2020, pp. 513-547.
[141] G. Zhang, H. Yuan, Y. Wang, K. Jiao, Applied Energy, 255 (2019) 113865.
[142] P. Schneider, C. Sadeler, A.-C. Scherzer, N. Zamel, D. Gerteisen, Journal of The Electrochemical Society, 166 (2019) F322-F333.
[143] G. Gu, J. Noh, I. Kim, Y. Jung, Journal of Materials Chemistry A, 7 (2019) 17096-17117.
[144] G. Fanourgakis, K. Gkagkas, E. Tylianakis, G. Froudakis, Journal of the American Chemical Society, 142 (2020) 3814-3822.
[145] N. Khajeh-Hosseini-Dalasm, S. Ahadian, K. Fushinobu, K. Okazaki, Y. Kawazoe, Journal of Power Sources, 196 (2011) 3750-3756.
[146] R. Ding, Y. Ding, H. Zhang, R. Wang, Z. Xu, Y. Liu, W. Yin, J. Wang, J. Li, J. Liu, Journal of Materials Chemistry A, 9 (2021) 6841-6850.
[147] M. Moein-Jahromi, M.J. Kermani, Energy Conversion and Management, 231 (2021) 113837.

[148] R. Ma, T. Yang, E. Breaz, Z. Li, P. Briois, F. Gao, Applied Energy, 231 (2018) 102-115.

[149] H. Lan, L. Yang, F. Zheng, C. Zong, S. Wu, X. Song, International Journal of Hydrogen Energy, 45 (2020) 12501-12513.

[150] B. Wang, B. Xie, J. Xuan, K. Jiao, Energy Conversion and Management, 205 (2020) 112460.

[151] R. Ding, W. Yin, G. Cheng, Y. Chen, J. Wang, R. Wang, Z. Rui, J. Li, J. Liu, Energy and AI, 5 (2021) 100098.